Semi-idealized urban heat advection simulations using the Weather Research and Forecasting mesoscale model

Bassett, Richard; Cai, Xiaoming; Chapman, Lee; Heaviside, Clare; Thornes, John

DOI:
10.1002/joc.5885

Received: 24 June 2017 | Revised: 1 October 2018 | Accepted: 4 October 2018

DOI: 10.1002/joc.5885

International Journal of Climatology RMetS

RESEARCH ARTICLE

Semi-idealized urban heat advection simulations using the Weather Research and Forecasting mesoscale model

Richard Bassett[1,2] | Xiaoming Cai[1] | Lee Chapman[1] | Clare Heaviside[1,3] | John E. Thornes[1,3]

[1]School of Geography, Earth and Environmental Sciences, University of Birmingham, Birmingham, UK

[2]Lancaster Environment Centre, Lancaster University, Lancaster, UK

[3]Chemicals and Environmental Effects Department, Centre for Radiation, Chemical and Environmental Hazards, Public Health England, Didcot, UK

Correspondence
Xiaoming Cai, School of Geography, Earth and Environmental Sciences, University of Birmingham, Edgbaston, Birmingham B15 2TT, UK.
Email: x.cai@bham.ac.uk

Funding information
Natural Environment Research Council, Grant/Award Number: NE/K008056/1; Birmingham City Council

Urban heat advection (UHA) can extend the climatic impact of a city into the surrounding countryside. This may lead to an intensification of already well-documented urban heat island (UHI) impacts on health and infrastructure, and challenge the representativeness of long-term reference temperature records taken near urban areas. However, previous UHA studies have been unable to accurately quantify surface-level UHA due to challenges arising from complex urban land-use patterns. To address this, the numerical Weather Research and Forecasting (WRF) mesoscale model coupled with the Building Energy Parameterization urban canopy scheme is used to simulate meteorological fields for idealized land-use cases. Hypothetical square cities (up to 32 km in size) are simulated for a year's period. A time-mean 2-m temperature field (representing the canopy UHI) shows that the mean UHI intensity (up to 4.3 °C [*SD* 1.7 °C]), wind speed <3.9 m/s) is linearly related to the logarithm of city size. This finding, entirely derived from numerical modelling, is consistent with the log-linear relationships previously found in the observational data of many cities in the world. A UHA methodology was then applied to the temperature fields to separate UHA from the UHI, with up to 2.9 °C (*SD* 1.7 °C) of UHA found downwind of the largest city size. For this hypothetical city size, an UHA intensity of 0.5 °C is found up to 24-km downwind from the urban boundary. In addition, the UHA-distance profiles along the central horizontal transect for various urban sizes are found to follow a scaling rule as a good approximation. As a result, the findings of this paper can be used as a starting point for climate impact assessments for areas surrounding urban areas without the need for complex, computation-intensive simulations.

KEYWORDS

BEP, mesoscale modelling, semi-idealized, urban heat advection, urban heat island, WRF

1 | INTRODUCTION

The urban heat island (UHI) is a zone (the "island") of warmer air and surface temperatures caused by differential heating and cooling rates between urban and rural land-use types. Typically, the air temperature in cities can be several degrees warmer than rural surroundings, and up to 10 °C in extreme cases (e.g. 7 °C Singapore, Chow and Roth, 2006; New York 8 °C, Gedzelman *et al*., 2003; Mexico City 8 °C, Jauregui, 1997; Vancouver 10 °C, Runnalls and Oke, 2000). The size of this temperature difference, the UHI intensity (UHII), is greatest at night under the conditions of clear skies and calm winds. UHII is a function of urban size and was originally demonstrated using population as a proxy for urban size (Oke, 1973; Park, 1986; Santamouris, 2015). This relationship has since been improved by using population

density (Steeneveld *et al*., 2011) that accounts for neighbourhood-scale UHII differences (i.e., two cities with the same population but covering different areas would have different urban morphologies and resulting UHIIs).

While the UHI can be beneficial, that is, reduced space heating requirements (Santamouris *et al*., 2001), the benefits are generally overshadowed by the negative effects of excess heat during summer. These include health risks, particularly during heatwaves (Stone *et al*., 2010; Heaviside *et al*., 2016); and infrastructure, for example, railway buckling (Chapman *et al*., 2013; Ferranti *et al*., 2016). The UHI may initiate thunderstorms (Bornstein and Lin, 2000; Dou *et al*., 2015) and increase precipitation (Shepard *et al*., 2002; Dixon and Mote, 2003). The UHI can also corrupt long-term climate records (Kalnay and Cai, 2003; Parker and Horton, 2005; Wickham *et al*., 2013; Koopmans *et al*., 2015). Therefore, understanding the dynamic, spatial nature of the UHI is particularly important to fully quantify risk due to the UHI. This is compounded by the fact that over half (and set to rise) of the world's population is now urbanized, and many areas are already at risk from a changing climate.

The transport of heat to areas downwind of the UHI by a horizontal wind flow is known as urban heat advection (UHA). While traditional theories suggest that the UHI is dispersed vertically to form an elevated urban plume (Oke, 1982), as supported by downwind airborne observations (Dirks, 1974; Wong and Dirks, 1978), UHA is also present at the near-surface level. This is due to (a) horizontal heat movement within the urban canopy layer (i.e., below roof level) and (b) downwind mixing of elevated heat downwards by turbulent eddies. Although surface-level UHA has been hypothesized for a while (Lowry, 1977) and acknowledged in several UHI studies (Brandsma *et al*., 2003; Unger *et al*., 2010; Brandsma and Wolters, 2012), UHA is rarely considered in UHI studies. This is in part due to a lack of spatial information caused by an observational paucity within the urban environment; the challenges associated with siting and maintaining urban meteorological networks are discussed in Muller *et al*. (2013) and Chapman *et al*. (2014). Another obstacle is the lack of an effective approach to enable UHA to be separated from UHI, because the air temperature at a given location is influenced by a combination of locally generated heat (i.e., due to underlying land use, topography and aspect) and the heat transported from upwind sources.

Nevertheless, recent observational (Bassett *et al*., 2016; Bassett *et al*., 2017a) and modelling (Heaviside *et al*., 2015; Bassett *et al*., 2017b) studies have overcome some of these challenges by developing and refining a methodology to separate UHA from the background UHI data. Detailed in the methodology, a time-mean temperature field (where all wind directions are considered) represents the background temperature, and a time-mean temperature field (for a chosen wind direction) represents the departure from the background temperature. For a given location with an upwind urban area, the difference between these two fields was attributed to the UHA.

This methodology was tested on a high-density urban observation network where a UHA intensity (UHAI) up to 1.2 °C was found for the city of Birmingham, UK (Bassett *et al*., 2016; details of the high-density urban observation network can be found in Warren *et al*., 2016). The UHA methodology was also shown to hold at a smaller (village) urban scale (Bassett *et al*., 2017a). However, although the UHA methodology was suitable to decompose temperatures into local and advected components at a local scale, it failed to account for regional heat advection (RHA). Due to the island nature of the UK where the methodology was developed, RHA may be particularly pronounced (i.e., large-scale coastal effects and topography). However, for modelling, this was overcome by conducting a second set of rural simulations that effectively removed any RHA effects (Bassett *et al*., 2017b).

While previous UHA studies were able to show the significance and general UHA spatial pattern, the exact UHAI was difficult to determine due to the complexity of spatial pattern of urban (and rural) land use. For example, temperature at a given location may be influenced by multiple upwind UHA sources. Furthermore, UHI processes occur across a range of scales. At smaller scales, shading from buildings or trees could introduce large temperature differences across street canyons that could exceed the UHAI. Additionally, these UHA studies hypothesized a symmetrical pattern between UHAI in opposing wind directions. However, the asymmetric urban land-use patterns used meant the results only partially matched this.

In order to address these issues caused by complex urban land use, this paper applies the non-hydrostatic Weather Research and Forecasting (WRF) model to semi-idealized urban land-use cases (i.e., simplifying the land use but retaining real meteorology). A similar approach was used to model the impact of a water body on a city (Theeuwes *et al*., 2013). WRF is a community-based model equipped with several urban parameterizations that have been extensively tested on the urban environment (Chen *et al*., 2011; Loridian *et al*., 2013). This paper presents the first study to apply the UHA methodology to simplified, idealized cities. The overall aim is to quantify how both the UHII and UHAI change with urban size. The results will be used to develop a simple statistical model that can be used to estimate UHAI without the need for computationally expensive simulations.

2 | METHODOLOGY

2.1 | WRF configuration

WRF (Skamarock *et al*., 2008) v3.8 was configured to run four 1-way nested domains at 3:1 grid ratios, with sizes 60×60 for domains 1–3 and 120×120 for the inner

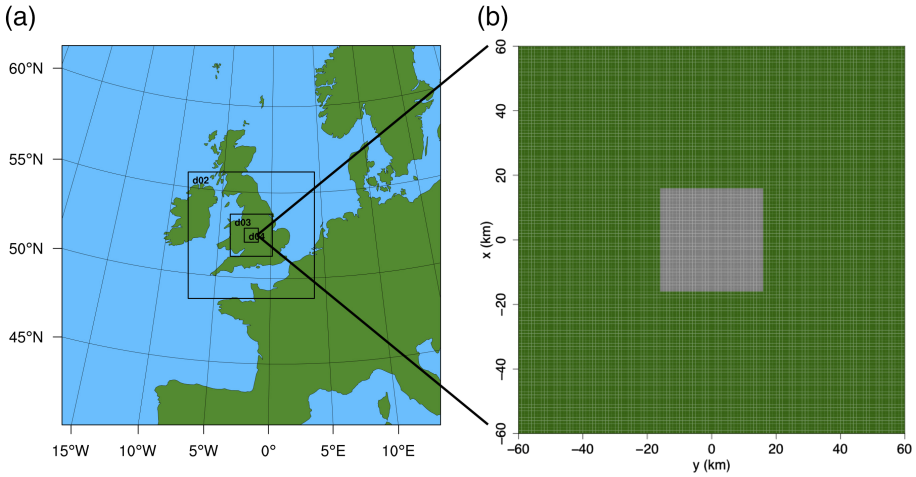

FIGURE 1 (a) WRF domain 1 (the outermost) to 4 (the innermost) configuration. (b) The black square represents the semi-idealized urban land-use (high-density residential) configuration in domain 4 for the 32 km case. The remainder of the domain was filled with the USGS land-use category 2, dryland cropland and pasture [Colour figure can be viewed at wileyonlinelibrary.com]

domain 4 (Figure 1a). The model was centred over Birmingham, UK (52.5°N, 1.9°W), the configuration already evaluated by Bassett *et al*. (2017b). The outermost domain covered northwest Europe at 27-km resolution and the innermost domain was set at 1-km resolution. The main reason for using a nested WRF configuration was to obtain reasonable, if not precise, synoptic weather conditions as the boundary conditions for the innermost domain, without significantly increasing computational time. The rapid radiative transfer model (Mlawer *et al*., 1997) was selected for longwave and the Goddard (Chou and Suarez, 1994) scheme for shortwave radiation. The Noah (Tewari *et al*., 2004) land surface model, which has four vertical soil layers, was used to represent natural surfaces, and for urban surfaces the multilayer Building Energy Parameterization scheme (BEP; Martilli, 2002) was employed. For the initial and boundary meteorological conditions, the NCEP (National Center for Environmental Prediction) FNL (Final) Operational Model Global Tropospheric Analyses data at 6-hr temporal and one degree horizontal resolution were used.

In order to simplify UHA, the complex urban land use associated with real cases was replaced with a single urban square centred in the innermost domain, as shown in Figure 1b. This follows a similar approach to Theeuwes *et al*. (2013) who demonstrated the suitability of using hypothetical land-use scenarios within a real modelling context. In total, six land-use configurations were created for the innermost domain: the first specifies a rural land use for the entire domain, whereas the others specify a squared urban land use surrounded by rural land use, with urban sizes (L_U) of 2, 4, 8, 16 and 32 km, respectively. An example of the 32-km urban size is presented in Figure 1b. A square land-use configuration was chosen because it would not be possible to create perfect circles using the WRF grid. For the urban simulations, the middle BEP urban land-use category, high-density residential, was used. The rural land use was set as "dryland cropland and pasture" in the USGS land-use categories. The urban fraction was set to one for the urban land use and zero for the rural land use. To avoid any undue effects from topography, for example, katabatic winds, the topography in the inner domain was flattened to sea level. Furthermore, to avoid any sudden step changes at the domain boundaries the topography was also set to 0 m in the other domains. It is expected that the simulations using flattened topography are not completely consistent, particularly in mountainous areas, with the initial conditions for all domains and boundary conditions specified in domain 1 from the NCEP model output. Therefore, this study was centred on Birmingham, UK, where topography is relatively flat. Additionally, the model output for domains 1, 2 and 3 with the flattened topography has shown (not presented here) that the meteorological fields (temperature, wind and pressure) are spatially smooth and in a dynamical balance after a couple of hours of spin-up time. Compared with simulations that adopt true topography, the key meteorological fields (wind, temperature, humidity and pressure) at the boundary of domain 4 are influenced by the flattened topography very little during the analysis periods.

The WRF-BEP configuration was run for a year (January 1 to December 31, 2013) for each land-use case. To account for model spin-up, the first 24 hr of each simulation were disregarded. Data were categorized into night and day, based on daily daylight lengths, and by cloud cover using 8 Oktas as a threshold (i.e., completely overcast), calculated using the WRF output variable CLDFRA. Based on nighttime clear sky data, wind was categorized into three equal groups, with resulting speeds of WG1 < 3.9 m/s, WG2 3.9–6.1 m/s and WG3 > 6.1 m/s. The resulting number of data hours for each category is listed in Table 1.

While it was not possible to directly evaluate simulated 2-m temperatures for the semi-idealized cases, a WRF-BEP configuration has been run for a real urban

TABLE 1 Mean UHII of all urban grid cells ($\overline{\Delta T'}$)

Clear night-time (°C)				Clear daytime (°C)			
	WG1 (n = 632)	WG2 (n = 632)	WG3 (n = 651)		WG1 (n = 435)	WG2 (n = 495)	WG3 (n = 985)
2 km	2.4 (1.2)	1.3 (1.0)	0.7 (0.3)	2 km	0.6 (0.8)	0.2 (0.4)	0.1 (0.3)
4 km	2.9 (1.4)	1.6 (1.2)	0.8 (0.4)	4 km	0.8 (0.9)	0.3 (0.5)	0.2 (0.3)
8 km	3.3 (1.5)	2.0 (1.3)	0.9 (0.5)	8 km	1.0 (1.0)	0.5 (0.6)	0.2 (0.4)
16 km	3.8 (1.6)	2.4 (1.4)	1.1 (0.6)	16 km	1.3 (1.2)	0.7 (0.7)	0.3 (0.4)
32 km	4.3 (1.7)	2.8 (1.5)	1.4 (0.8)	32 km	1.7 (1.3)	1.0 (0.9)	0.5 (0.5)
Cloudy night-time (°C)				**Cloudy daytime (°C)**			
	WG1 (n = 470)	WG2 (n = 484)	WG3 (n = 1,271)		WG1 (n = 447)	WG2 (n = 663)	WG3 (n = 1,115)
2 km	1.7 (1.8)	0.5 (0.7)	0.4 (0.2)	2 km	0.7 (0.9)	0.2 (0.4)	0.1 (0.3)
4 km	2.0 (2.1)	0.7 (0.8)	0.4 (0.2)	4 km	0.9 (1.1)	0.3 (0.5)	0.2 (0.3)
8 km	2.4 (2.3)	0.9 (0.9)	0.5 (0.3)	8 km	1.1 (1.2)	0.4 (0.6)	0.3 (0.4)
16 km	2.7 (2.5)	1.1 (1.1)	0.6 (0.4)	16 km	1.4 (1.4)	0.6 (0.7)	0.4 (0.4)
32 km	3.2 (2.7)	1.4 (1.2)	0.8 (0.5)	32 km	1.8 (1.6)	0.9 (0.8)	0.5 (0.6)

Note. WG1: <3.9 m/s, WG2: 3.9–6.1 m/s and WG3: >6.1 m/s. The standard deviations are presented in brackets.

case and evaluated (Bassett *et al*., 2017b). A mean root-mean-square error (RMSE) of 1.68 °C and mean bias error (MBE) of −0.33 °C across 32 stations (both urban and rural) were found in this previous study. It was suggested that statistical differences could be due to comparisons between point observations (that may be affected by sub-grid scale processes) and the 1-km model resolution.

2.2 | UHI and advection

Techniques developed through observational (Bassett *et al*., 2016; Bassett *et al*., 2017a) and modelling studies (Heaviside *et al*., 2015) have shown that the temperature at a given location was a combination of (a) heat generated locally (i.e., determined by the underlying land use) and (b) heat advected from upstream urban sources. Further analysis by Bassett *et al*. (2017b) showed that the derived UHAI results contained RHA. A methodology to separate UHA from RHA was consequently developed and contained two stages: (Stage I) total urban heat (UHI and UHA) was separated from background regional temperature field (i.e., the rural simulation), and (Stage II) UHA was separated from the UHI. A hypothetical illustration to explain this approach is provided in Figure 2 and explained below.

The results of hypothetical urban (T_{urban}) and (single) rural (T_{rural}) simulations for the selected categories (e.g., wind speed, see section 2.1 for the details) were analysed to derive UHI and UHA temperature fields, for each of the five urban cases, in which L_U = 2, 4, 8, 16, 32 km. In Stage I, by subtracting the rural case (T_{rural}) from each of the five urban (T_{urban}) cases, the resulting pattern depicts the UHII field at each hour (ΔT), and where all hours were considered (i.e., combining all categories described in section 2.1) the time-mean ($\overline{\Delta T}$), indicated in Equation (1). This is illustrated hypothetically in the top row of Figure 2. Each simulation hour was then categorized into one of the four directions (θ) using the cross-domain mean 10-m wind direction. The same calculation as (a) was then applied to the hourly UHII field categorized into wind directions, with the time-mean UHII field ($\overline{\Delta T^{\theta}}$), indicated by Equation (2). This shows how the resulting time-mean UHII field ($\overline{\Delta T^{\theta}}$) was modified by wind direction (illustrated in the middle row of Figure 2). The resulting UHII field for each wind direction was then rotated to align to a westerly, and then the mean of these four directional rotated UHII fields was taken, represented as $\overline{\Delta T^{\bar{\theta}}}$.

$$\overline{\Delta T} = \frac{\Sigma\left(T_{\text{urban}} - T_{\text{rural}}\right)}{n}, \tag{1}$$

$$\overline{\Delta T^{\theta}} = \frac{\Sigma\left(T^{\theta}_{\text{urban}} - T^{\theta}_{\text{rural}}\right)}{n}. \tag{2}$$

The operations of (1) and (2) have been shown to remove RHA effects, while retaining UHA information (Bassett *et al*., 2017b). An example why this approach was used is that a strong regional temperature gradient within domain 4 under, for example, a northerly wind flow would be present in both the urban and rural simulations. By subtracting the northerly wind flow rural case from the urban case, the resulting field (e.g., $\overline{\Delta T}$) has effectively removed any regional effect (as these were contained in both simulations).

In Stage II, to isolate the UHAI effect, the time-mean UHII field ($\overline{\Delta T}$) was subtracted from the UHI field at each hour, classified by wind direction (ΔT^{θ}), before calculating the time-mean ($\overline{\Delta T^{\theta}}$), as shown in Equation (3), for each of the five urban sizes. This is shown hypothetically in the bottom row of Figure 2, that is, whether the downwind air temperature for a given wind direction is warmer or cooler than if the mean downwind temperature was calculated using all wind directions,

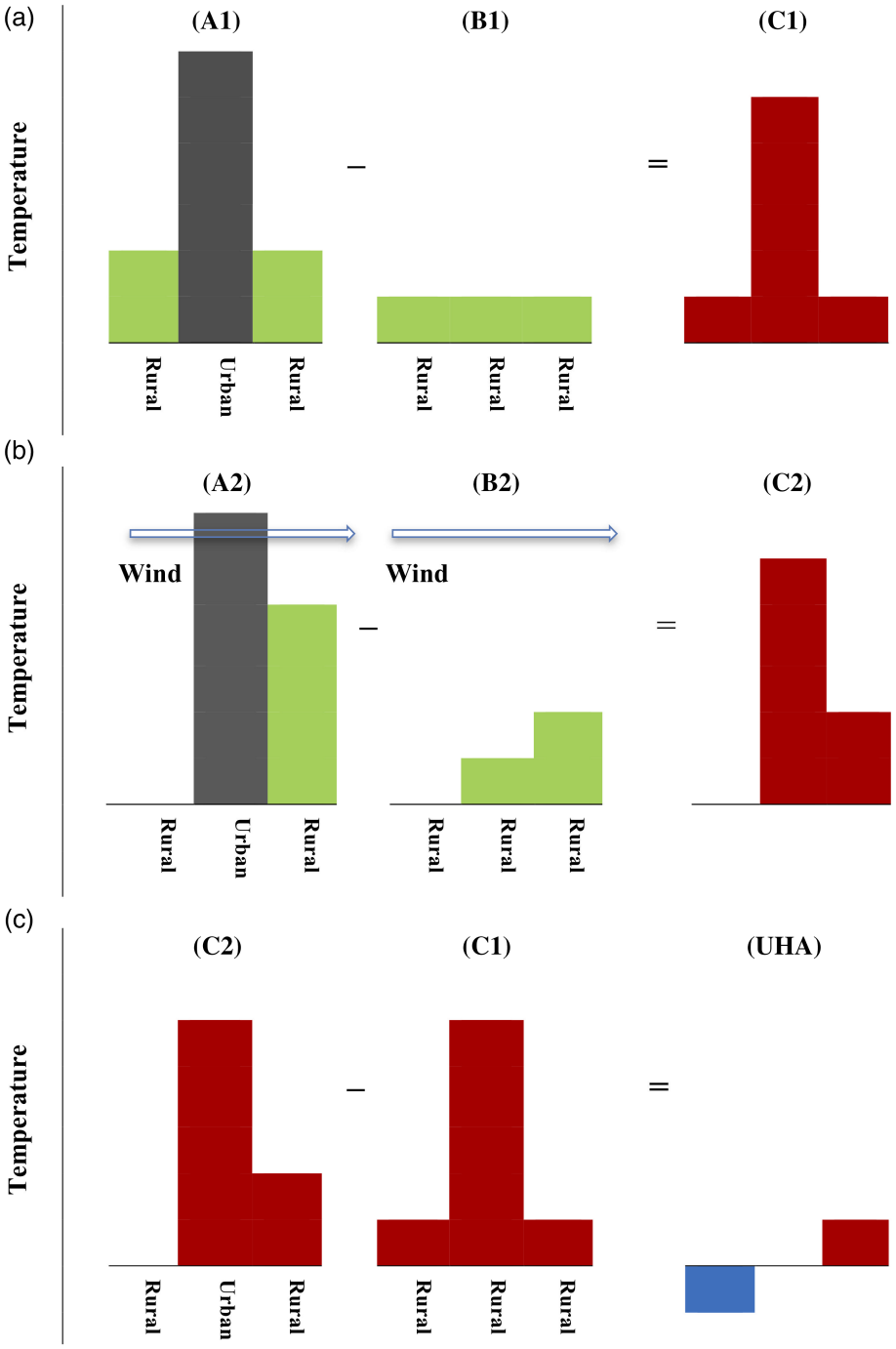

FIGURE 2 Hypothetical UHA calculation that excludes RHA effects. Diagrams named with (a) are for elevated temperatures due to RHA + UHA (i.e., output of the idealized urban simulations), (b) for elevated temperatures due to RHA only (i.e., output of the rural simulations), and (c) for the difference between (a) and (b) (i.e., elevated temperatures due to UHA only). In the top row, all wind directions (i.e., wind from left to right and right to left) were considered, and the resulting pattern (C1) represents the time-mean UHII field ($\overline{\Delta T}$). In the middle row, only one wind direction (i.e., wind from left to right) is considered, and the resulting (C2) represents the directional time-mean UHII field ($\overline{\Delta T^{\theta}}$). In the bottom row, (C2) and (C1) are copied from above, and (C2)–(C1) yields (UHA), which is the UHA field ($\overline{T^{\theta}_{\mathrm{UHA}}}$) that is free from the local-UHI and RHA effect [Colour figure can be viewed at wileyonlinelibrary.com]

$$\overline{T^{\theta}_{\mathrm{UHA}}} = \frac{\Sigma\left(\Delta T^{\theta} - \overline{\Delta T}\right)}{n}. \quad (3)$$

The UHA methodology is further adapted to use only two opposing wind directions when creating the time-mean UHII ($\overline{\Delta T}$): (a) mean of north and south, and (b) mean of east and west. This step was taken because the land-use configurations for the urban cases are symmetrical (i.e., square), therefore removing any noise from adjacent wind directions that were not being analysed. The approach taken to rotate the UHII field ($\overline{\Delta T^{\theta}}$) to a single direction was also applied to the UHAI results. This was achieved by flipping (as the land-use is symmetrical) the northerly UHAI

field, then taking the mean with the southerly UHAI field. The same approach was then applied to the east and west UHAI fields. The resulting two UHAI fields were then rotated to the same (westerly) direction and the mean was taken. The result, $\overline{T^{\theta}_{\mathrm{UHA}}}$, is effectively the mean UHAI field of all wind directions.

Results from previous studies (Heaviside *et al*., 2015; Bassett *et al*., 2016; Bassett *et al*., 2017a; 2017b) showed UHAI ($\overline{T^{\theta}_{\mathrm{UHA}}}$) to be negative upwind and positive downwind, a product of the methodology. A negative UHAI component at a location upwind of the city does not refer to cooling, but reflects the advected heat which is induced by the wind flow from the opposite direction and is hidden inside $\overline{\Delta T}$; once Equation (3) is applied to this location, because upwind $\overline{\Delta T^{\theta}}$ contains zero temperature elevation but upwind $\overline{\Delta T}$ contains a positive elevated temperature, this gives a negative value for $\overline{T^{\theta}_{\mathrm{UHA}}}$. Therefore, as illustrated by the bottom row of Figure 2, the total UHAI component was interpreted as the difference between positive and negative values. However, it is noted that within the urban land use, cooling may be present from the surrounding rural land use (i.e., the opposite effect to UHA) and this is out of the scope of this study.

3 | RESULTS AND DISCUSSION

3.1 | Semi-idealized UHI

The modelled time-mean UHII fields ($\overline{\Delta T}$, as illustrated by [C1] in the top diagram of Figure 2) for the five urban size cases are shown in Figure 3a, where it is clear that an increase in UHI area and intensity are related to an increase in urban size (L_U). In order to explore this relationship, the mean $\overline{\Delta T}$ of all urban grid cells is taken for each case, noted as $\overline{\Delta T'}$ (e.g., for the 4 km case $\overline{\Delta T'}$ is the mean of 16 urban grid cells) and interpreted as the average UHII of the urban square. $\overline{\Delta T'}$ was found to increase with urban size, for WG1 (<3.9 m/s): 2.4 °C (*SD* 1.2 °C), 2.9 °C (*SD* 1.4 °C), 3.3 °C (*SD* 1.5 °C), 3.8 °C (*SD* 1.6°C) and 4.3 °C (*SD* 1.7 °C) for the 2–32 km cases, respectively. The corresponding 95th percentile UHII (ΔT^{P95}) values were 4.3, 5.0, 5.6, 6.3 and 7.0 °C. The distribution of night-time UHII for each wind speed group is presented in Figure 3c, where a decrease in UHII is found with increasing wind speed from WG1 to WG2, and similar decrease moving to WG3. The mean UHII values during the day and for cloudy conditions are listed in Table 1. Notably, a reduction in UHII is found with either cloudy conditions or during the day. During the day, cloud does not have much impact on UHII.

The relationship between mean UHII ($\overline{\Delta T'}$) and the urban size was found to follow a logarithmic law, similar to that observed by Oke (1973), who showed that long-time maximum UHIIs, observed across a range of large U.S. and European cities, were linearly related to log of city population (i.e., a proxy for urban size). To compare the semi-idealized urban results with real cases for the European cities from Oke (1973) urban size (L_U) was estimated using a population density of 3,000 people per km^2 (based on the West Midlands region, Birmingham City Council, 2011). The UHII data for the European cities from Oke (1973) is plotted alongside the 95th percentile idealized UHII results for WG1 (ΔT^{P95}) in Figure 3b. The resulting relationship (for WG1) can be represented through a simple linear regression ($R^2 = 0.99$):

$$\Delta T^{P95} = 0.95\,(\log L_U) + 3.68, \tag{4}$$

where log denotes the natural logarithm. The UHII results from the present study are comparable to that found by Oke (1973). Differences in slope may be explained by the WRF-BEP configuration, for example, anthropogenic heat sources were not considered and only the middle WRF-BEP urban land-use type was used. Spatially, a subtle warming was noted in the rural areas directly surrounding the urban areas and is indicative of the UHA effects. However, it is difficult to visualize UHA in the UHII plots as the signal is obscured by the overall UHI pattern. Finally, it is important to note these values of UHII were derived from a single urban category that does not reflect all urban land-use variability within real urban areas. For example, this semi-idealized case may not be translated directly to real cases, due to complexity caused by different urban geometries, construction materials and vegetation quantities.

3.2 | Semi-idealized UHA

Although it appears from the time-mean UHII field ($\overline{\Delta T}$) presented in Figure 3a that the majority of the UHI was contained within the urban land-use boundary, there was evidence of heat transport outwards from the urban into rural areas. In order to visualize this clearly, and before the UHA methodology was applied, an example of the directional UHII ($\overline{\Delta T^{\theta}}$) is presented on a horizontal slice in Figure 4a and on a vertical slice in Figure 4b for the 32-km urban size. For the horizontal UHII, several notable features were observed for the directional UHII. First, the location of the peak UHII was shifted from the centre to near the downwind boundary of the urban land use and the intensity was greater than the all direction cases (Figure 3a). Next, the advection of heat from the urban into the downwind rural area was evident, peaking in the rural grid cells closest to the downwind edge of the city. Lastly, a lower UHII was noted on the inside upwind edge of the city, due to advected cool rural air (a similar process to UHA). It was also noted that the heat pattern extending from the urban into the rural land use is curved. This was due to the use of real meteorology, that is, the four wind directions each contained wind flows in a 90° arc. The advected plume

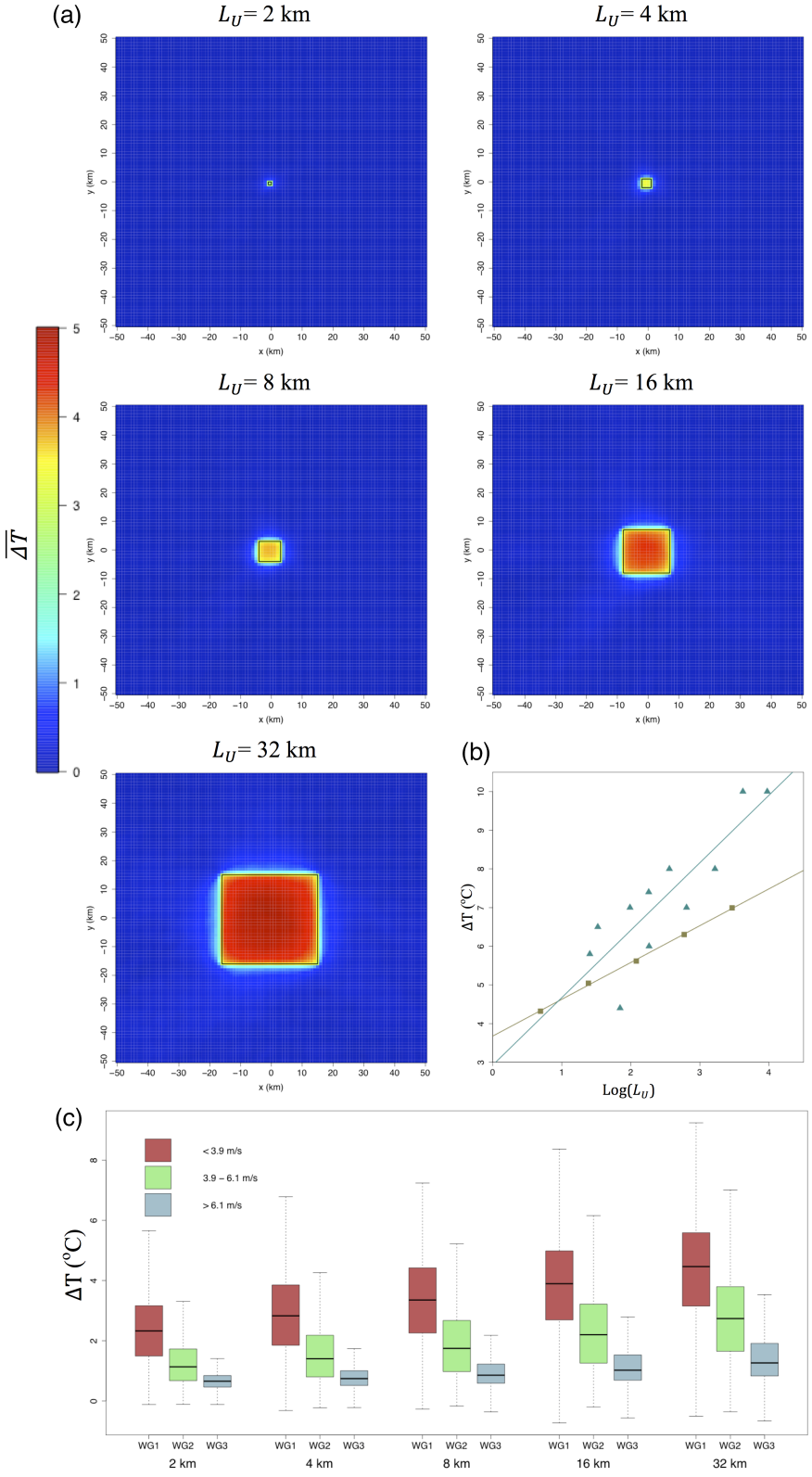

FIGURE 3 (a) Domain 4 time-mean 2-m UHII field ($\overline{\Delta T}$) for each urban size (L_U = 2, 4, 8, 16, 32 km) where all wind directions are used. The results shown are for clear, night-time, WG1 (<3.9 m/s) conditions. The black box shows the outer boundary of the urban land use. (b) The relationship between the 95th percentile UHII, ΔT^{P95}, and the log urban size (L_U) is given in brown squares; $\Delta T^{P95} = 0.95\ (\log L_U) + 3.68$. A comparison with Oke's (1973) relationship between urban size (converted from population) and maximum UHII for European cities is shown in light blue triangles. (c) The distribution of UHII for each modelled urban size and wind group. The whiskers represent 1.5 × IQR range, outliers are not shown [Colour figure can be viewed at wileyonlinelibrary.com]

from the cities was similar in appearance to the cooling effect found modelling idealized urban lakes (Theeuwes *et al.*, 2013). For the vertical UHII, (Figure 4b), the UHI exhibits a typical plume pattern, with heat propagating vertically into the boundary layer. This elevated plume was shown to extend furthest downwind under WG2, where a mean vertical warming

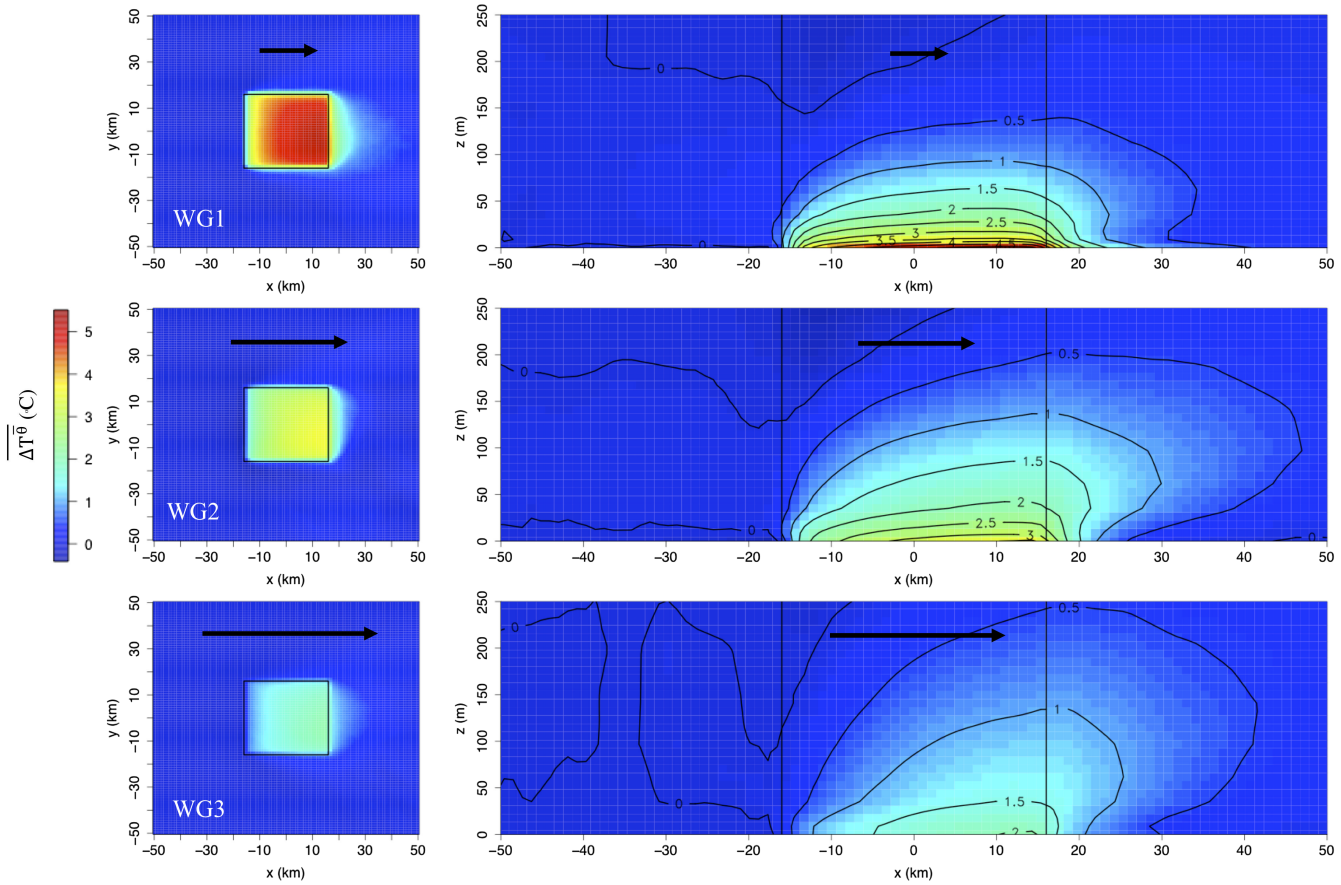

FIGURE 4 (a) Left-hand side: directional time-mean 2-m UHII ($\overline{\Delta T^{\bar{\theta}}}$) calculated as the rotated mean of the N, S, E and W wind direction UHII fields for the 32-km urban size (clear sky, night-time) for WG1: <3.9 m/s, WG2: 3.9–6.1 m/s and WG3: >6.1 m/s. The black arrow represents the mean 10-m wind direction and black box shows the outer boundary of the urban land use. (b) Right-hand side: vertical transect profile of $\overline{\Delta T^{\bar{\theta}}}$ taken for each wind group on the left-hand side at $y = 0$. The vertical lines represent the urban boundary [Colour figure can be viewed at wileyonlinelibrary.com]

of 1 °C was modelled to approximately 135 m above the surface, extending 14 km downwind and 0.5 °C modelled to 200 m, extending 31 km downwind. Although Figure 4b highlights that heat from cities also propagates vertically downwind, the UHA analysis presented herein is limited by the methodology to the surface only.

While Figure 4a shows heat from the UHI advected into the downwind rural area, it does not clearly differentiate between the UHAI and UHII fields. In order to separate the UHA effects, the UHA methodology described in ection 2.2 was applied. The resulting time-mean UHAI field, denoted as $\overline{T^{\bar{\theta}}_{\mathrm{UHA}}}$, is presented as a single direction that contains information of all wind directions (similar to Figure 4a) in Figure 5. The results show that UHA is present for each urban size. Visually, the UHAI and area of influence increases with each urban size increment. The downwind positive UHAI, over 1°C for the 16 km case, shows the majority of the effect to occur outside the urban boundary. Notably, the negative and positive UHA effects are symmetrical for each urban size. This has been discussed in Section 2.2 and matches the hypothetical methodology shown in Figure 2. This symmetry was unattainable in previous applications of the UHA methodology (Heaviside *et al.*, 2015; Bassett *et al.*, 2016; 2017b) due to complex land-use patterns.

To explore the characteristics of the UHAI ($\overline{T^{\theta}_{\mathrm{UHA}}}$) shown in Figure 5, a horizontal transect (left to right) was taken through the centre of each urban area. These transects are presented as boxplots containing all hourly data for the 32 km case in Figure 6a and time-mean values for all urban sizes in Figure 6b. As discussed in the methodology, the total UHAI ($\overline{T^{\bar{\theta}}_{\mathrm{UHA}}}$) is the difference between the negative and positive UHAI values, and it is these differences that are presented in Figure 6. The "splinefun" package in R was used to cubically interpolate the UHAI between the 1-km WRF grid spacing in Figure 6b. Using this spline interpolation the results show the UHAI ($\overline{T^{\theta}_{\mathrm{UHA}}}$) increases with distance from the urban centre, until peaking directly after the urban land-use boundary (indicated by the vertical lines in Figure 6b). This peak UHAI occurred at a mean distance of 1.3 km from the urban boundary (i.e., the adjacent rural grid cell), before decreasing with distance. A maximum mean UHAI for WG1 (<3.9 m/s) of 2.9 °C (*SD* 1.7 °C) was modelled for the 32-km urban size. This value corresponds to the same level of advected UHI in the immediate downwind

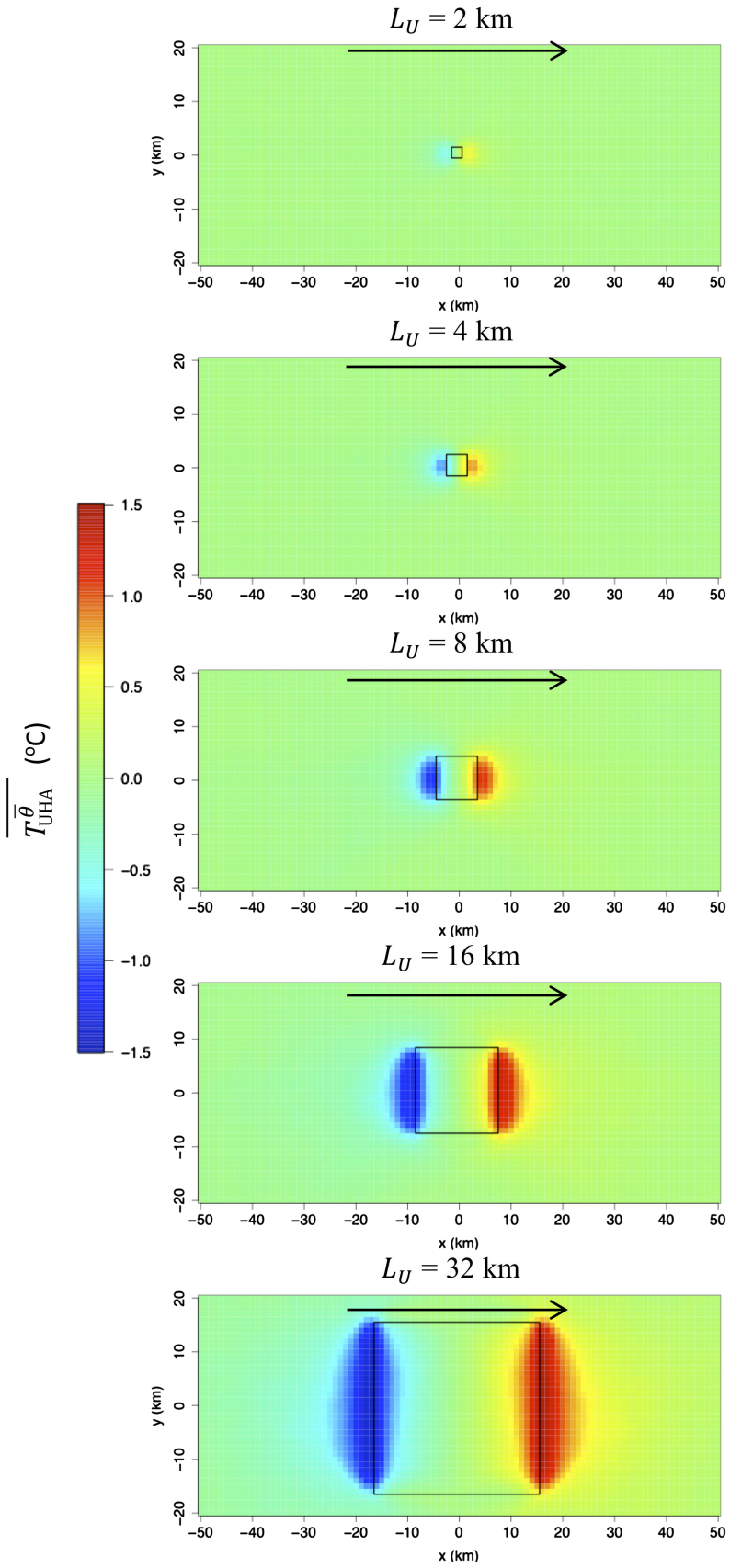

FIGURE 5 Rotated time-mean UHAI field ($\overline{T^{\bar{\theta}}_{\mathrm{UHA}}}$) for each idealized urban size (L_U). The black rectangle in each plot represents the urban outline, and black arrow the wind direction (clear sky, night-time, WG1: <3.9 m/s) [Colour figure can be viewed at wileyonlinelibrary.com]

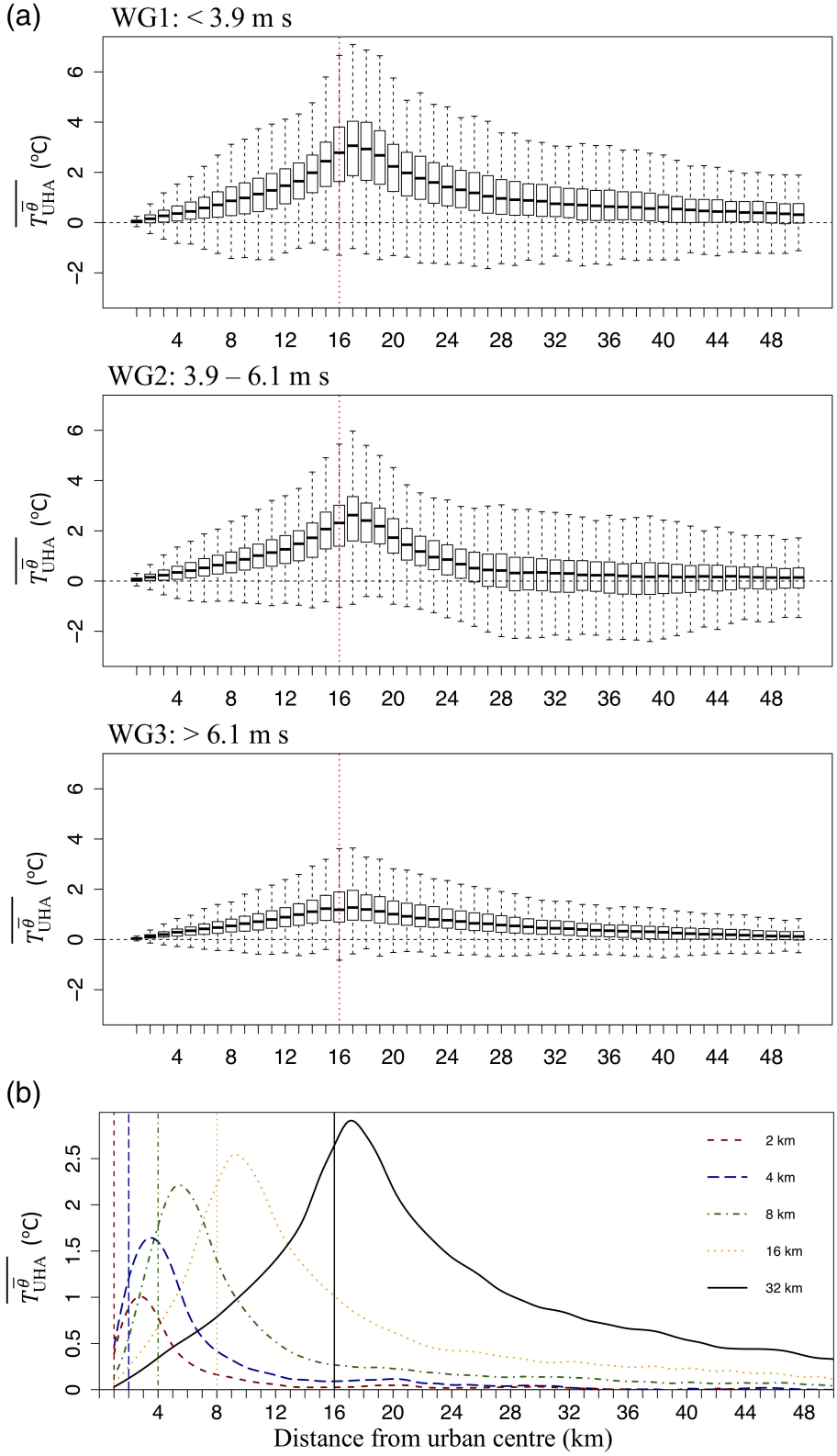

FIGURE 6 (a) Transect showing UHAI at $y = 0$ (see Figure 5) for the 32-km city for each wind speed group (clear sky, night-time). Each box plot contains hourly rotated data of all wind directions and is the difference between negative and positive UHA. The whiskers represent 1.5 × IQR range and red line the urban–rural boundary. Outliers are not shown. (b) Horizontal transects through the rotated time-mean directional UHAI fields ($\overline{T^{\bar{\theta}}_{UHA}}$) for each urban size in WG1 (clear sky, night-time). The negative and positive UHAI values from Figure 5 were combined to show the total UHAI contribution. Spline interpolation was used to smooth each UHAI transect caused by the 1-km WRF grid spacing. The vertical lines represent the rural–urban boundary for each city size [Colour figure can be viewed at wileyonlinelibrary.com]

rural areas shown in the earlier directional UHII result (Figure 4b), providing further justification to combine the negative and positive UHAI values. The results for each urban size and wind speed groups are presented in Table 2a. UHA is shown to extend considerably from the urban–rural boundary for each urban size, as shown for

32 km case in Figure 6a. The mean distances for all urban sizes are quantified in Table 2b,c. For example, the 16-km urban case has a 0.5 °C UHAI extending up to 13 km from the urban boundary, and 32 km case up to 24 km.

3.3 | Scaled UHA statistical model

The similarity of the profiles of the UHAI transects shown in Figure 6b suggests that it may be feasible to create a simple statistical model to fit all the profiles. The intention is to provide a means to calculate UHAI without the need to run intensive computer simulations. In order to accomplish this, the main factors affecting UHAI need to be explored statistically. Linear regression was used to show the relationship between distance (D) that the peak UHAI value is found ($D_{\max}$) and urban size (L_U). A significant relationship ($R^2 = 0.99$) was found, shown in Figure 7a and Equation (5). The same approach was then applied to the relationship between the UHAI maximum ($\overline{T^{\bar{\theta}}_{\text{UHA max}}}$) and log($L_U$). This subsequently yielded a significant linear relationship shown in Figure 7b and Equation (6) ($R^2 = 0.98$).

$$D_{\max} = 0.48\,L_U + 1.63, \tag{5}$$

$$\overline{T^{\bar{\theta}}_{\text{UHA max}}} = 0.68\log(L_U) + 0.65. \tag{6}$$

We can then adopt the following scaling approach: (a) the distance from urban centre, D, is scaled by $D_{\max}$, and (b) the UHAI value ($\overline{T^{\bar{\theta}}_{\text{UHA}}}$) at each distance is scaled by the peak UHAI ($\overline{T^{\bar{\theta}}_{\text{UHA max}}}$). The profiles of UHAI transects, expressed by two new scaled variables, $D' = D/D_{\max}$, and $\overline{T^{\theta'}_{\text{UHA}}} = \overline{T^{\bar{\theta}}_{\text{UHA}}}/\overline{T^{\bar{\theta}}_{\text{UHA max}}}$, are presented in Figure 7c. It is clear that the UHAI transects for each urban size show a close resemblance. The log of the resulting transformed mean transect (i.e., D'' is at 0.1 resolution from the five curves at D') is illustrated in Figure 7d. These steps are summarized in Equations (7) and (8)

$$D'' = \log\left(\frac{D}{D_{\max}}\right), \tag{7}$$

$$\overline{T^{\theta''}_{\text{UHA}}} = \log\left(\frac{\overline{T^{\bar{\theta}}_{\text{UHA}}}}{\overline{T^{\bar{\theta}}_{\text{UHA max}}}}\right). \tag{8}$$

A Fourier series was then used to approximate the log relationship of the mean transformed transect curve ($\overline{T^{\bar{\theta}''}_{\text{UHA}}}$) as expressed in Equation (9). The parameters for this equation were estimated using the nonlinear least squares function in R.

$$\overline{T^{\bar{\theta}''}_{\text{UHA}}} = -3.33 + 2.66\cos\left(D''\right) + 0.46\cos\left(2D''\right) - 1.49\sin\left(D''\right) + 0.60\sin\left(2D''\right) - 0.026\sin\left(3D''\right). \tag{9}$$

The information generated through fitting the UHAI transects from different urban sizes has therefore formed a simple UHAI statistical model. For any given urban size L_U and distance D, the surface-level UHAI value can be estimated using this methodology. The UHAI transects that the model outputs along with the original modelled cases are shown in Figure 7e. The statistical model is able to satisfactorily replicate the modelled urban cases; however, the peak UHAI is slightly underestimated. While this methodology is derived for a simplified urban case, and does not show all urban complexities (or variation in meteorology), it can be used as a simple means to estimate UHAI. However, this approximation is based on a single land-use type and wind speeds <3.9 m/s. The statistical model is also based on a standalone square urban area (i.e., does not consider the interactions, perhaps nonlinear, between multiple urban areas) and does not contain vegetation (therefore UHA results may be higher than expected in reality). Addressing these issues could form the base of future research.

TABLE 2 (a) Mean UHAI ($\overline{T^{\bar{\theta}}_{\text{UHA}}}$) at the downwind grid cell adjacent to the urban–rural boundary for clear-sky, night-time conditions. (b) Downwind distance from the urban–rural boundary at which a mean UHAI greater than 1 C is found. (c) The same as (b) but for UHAI greater than 0.5 C. WG1: <3.9 m/s, WG2: 3.9–6.1 m/s and WG3: >6.1 m/s

(a)	WG1 (°C)	WG2 (°C)	WG3 (°C)
2 km	0.8 (0.9)	0.5 (0.8)	0.1 (0.2)
4 km	1.5 (1.2)	1.0 (1.0)	0.3 (0.4)
8 km	2.1 (1.3)	1.5 (1.1)	0.6 (0.6)
16 km	2.5 (1.4)	2.0 (1.2)	1.0 (0.7)
32 km	2.9 (1.7)	2.5 (1.4)	1.4 (0.9)
(b)	**WG1 (km)**	**WG2 (km)**	**WG3 (km)**
2 km			
4 km	3	1	
8 km	5	3	
16 km	7	5	
32 km	11	7	5
(c)	**WG1 (km)**	**WG2 (km)**	**WG3 (km)**
2 km	3	2	
4 km	5	3	
8 km	7	5	3
16 km	13	8	8
32 km	24	10	14

Note. The standard deviations are presented in brackets.

4 | CONCLUSIONS

Previous attempts to quantify UHA were hampered by complex urban land-use patterns. To overcome this, semi-idealized simulations (five urban and one rural), a year each in length, were conducted using the WRF-BEP mesoscale model configuration. Within the inner model domain, the

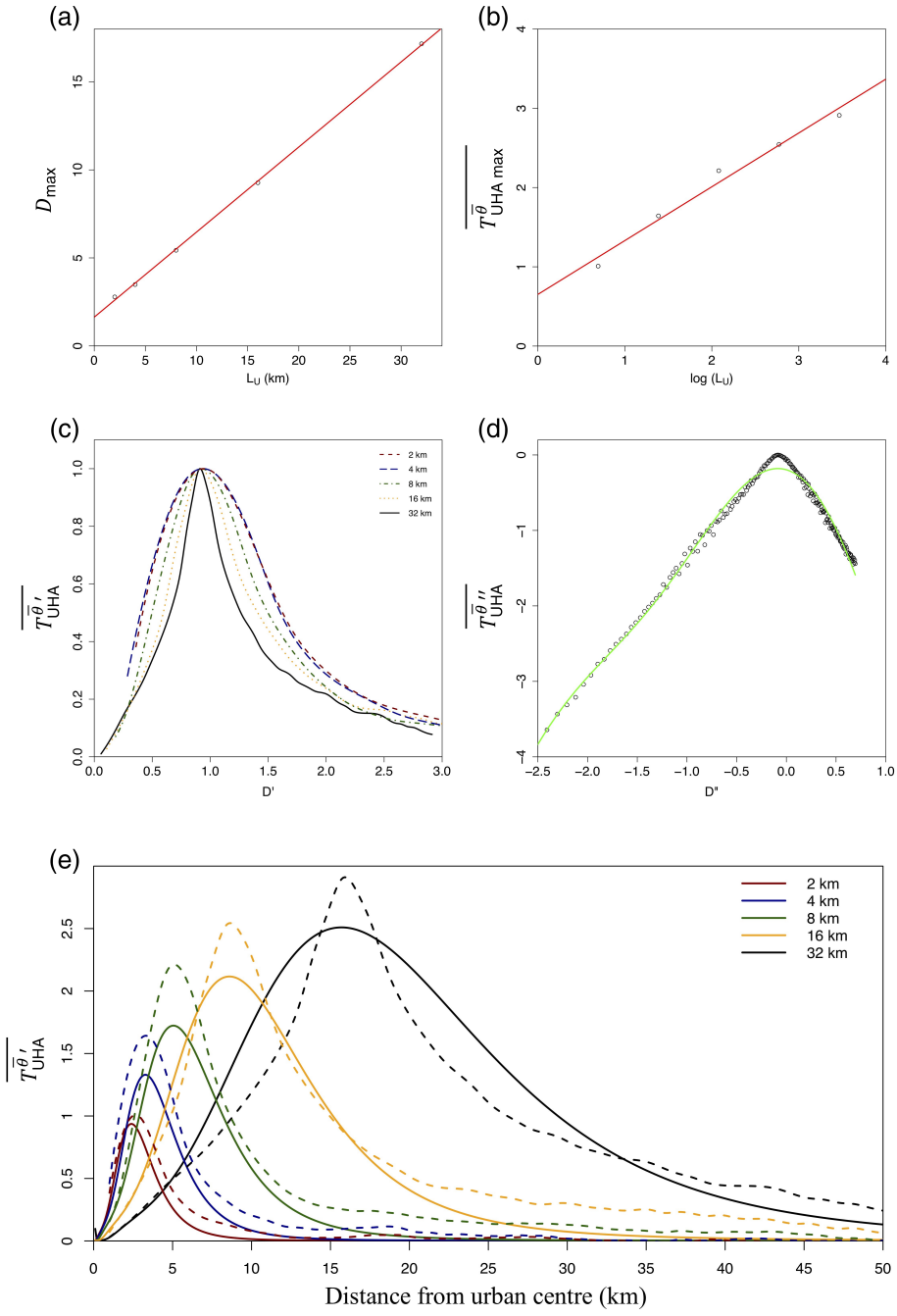

FIGURE 7 (a) The relationship between urban size (L_U) and peak UHAI distance from the urban centre (D_{max}). The equation of the line is given at (5). (b) Relationship between log urban size (L_U) and peak UHAI ($\overline{T^{\bar{\theta}}_{UHA\ max}}$). The equation of the line is given at (6). (c) Decomposed UHAI transects (the original transects are shown in Figure 6b). (d) Log mean of the collapsed UHAI transects found in Figure 7c shown in dots. The equation of the Fourier line is given at (9). (e) UHAI statistical model output for L_U = 2, 4, 8, 16 and 32 km are shown solid lines and the original modelled output in dashed lines. All relationships in Figure 4 are for clear sky, night-time and WG1 (<3.9 m/s) [Colour figure can be viewed at wileyonlinelibrary.com]

land use was replaced with simplified, square, representations of cities up to 32 km in size. A rural only land-use simulation was also conducted and used to remove any non-urban, RHA effects from the results. From this, a time-mean 2-m temperature field was calculated as the difference between each urban and rural simulation considering: (a) all wind directions and (b) directional cases.

The all wind direction time-mean UHII field had a temperature difference between the urban and rural simulations up to 4.3 °C (WG1: <3.9 m/s) for the hypothetical 32-km urban size. The UHII was found to be related to the logarithm of urban size, in agreement with the observational analysis conducted by Oke (1973). For the directional UHII cases, a clear pattern of heat transport from the urban to rural land use (as well as advection of cool rural air into the city) was shown. The spatial location of the peak UHII was found to intensify and move to the (inside) downwind boundary of the urban land use.

UHA was separated from the underlying UHII, resulting in a clear UHA field free from complexities caused by real land-use patterns. A horizontal transect was taken through each UHAI field. This showed symmetrical negative and positive UHAI values (opposing wind directions) that were subsequently combined to derive the downwind-only UHAI field. This addition created the same UHAI as found with the earlier advected UHII results. The results (for WG1: <3.9 m/s) showed a UHAI up to 2.9 °C for the hypothetical 32-km urban size. The largest UHAI were found in the downwind rural grid cell directly adjacent to the urban boundary (i.e., 1 km away). A UHAI effect of 0.5 °C was found to extend up to 24-km downwind of the urban boundary for the 32-km urban size. A significant UHAI, 0.8 °C (*SD* 0.9 °C), was initiated by the smallest urban size, 2 km. While a 2.9 °C UHAI (32-km urban size) appears large and double that found in observations (Bassett *et al*., 2016), the urban land use in these simulations did not contain vegetation (i.e., urban fraction was set to 1). This is in contrast to (the majority of) real cities where vegetation (including urban parks) and moisture would reduce the overall UHAI.

The maximum UHAI was related to the log urban size (similar to the UHII), and the distance at which this maximum UHAI occurred was linearly related to the urban size. Using this scaling rule, all UHAI transects for the five tested urban sizes were collapsed on top of one another reasonably well. As each transect (once collapsed) was similar to one another, this information was used to create a predictive statistical UHAI model. The model takes an input of urban size, and estimates the downwind UHAI with distance. This statistical UHAI model has practical benefits, for example, it may be used to estimate UHAI in areas not currently considered at risk, that is, outside the traditional UHI concept. The potential to assess the extent of UHA "contamination" by nearby urban settlements has benefits for the climate community. For instance, knowledge that a city of *x* km size has a UHA influence *y* km from the city limit could be applied to the global climate observing system to enhance station classifications from simply urban and rural. Currently urban stations are preferentially avoided in climate analysis because of known effects on air temperature. However, if rural stations have inaccurate classifications due to UHA, this may lead to biases in the background climate signal (also leading to an underestimate of UHII). Results from this study could be put into practice to help identify these stations where UHA is present. Further work may be taken to extend this research by (a) creating more complex idealized urban representations, that is, an urban area upwind of another urban area, (b) testing different urban land-use types, and (c) using fully idealized weather conditions could be used to control wind speed and direction. This would enable interpretation of UHA under different weather scenarios.

Overall, this paper has shown that simplifying urban land use in WRF substantially improves quantification of UHA. This work builds on and provides justification to a UHA methodology that was not previously fully tested due to the complexities of urban land use. It is anticipated that the statistical UHAI model developed from the results can be used as a tool to help mitigate UHI and UHA impacts.

ACKNOWLEDGEMENTS

This research was principally supported by a Natural Environment Research Council CASE (collaborative award in science and engineering) studentship (Grant No. NE/K008056/1) and partly funded by Birmingham City Council. The computations described herein were performed using the University of Birmingham's BlueBEAR HPC service (http://www.bear.bham.ac.uk).

ORCID

Richard Bassett https://orcid.org/0000-0002-5334-7951
Xiaoming Cai https://orcid.org/0000-0002-5934-9800

REFERENCES

Bassett, R., Cai, X.-M., Chapman, L., Heaviside, C., Thornes, J.E., Muller, C.L., Young, D.T. and Warren, E.L. (2016) Observations of urban heat island advection from a high-density monitoring network. *Quarterly Journal of the Royal Meteorological Society*, 142, 2434–2441. https://doi.org/10.1002/qj.2836.

Bassett, R., Cai, X.-M., Chapman, L., Heaviside, C. and Thornes, J.E. (2017a) The effects of heat advection on UK weather and climate observations in the vicinity of small urbanized areas. *Boundary-Layer Meteorology*, 165, 181–196. https://doi.org/10.1007/s10546-017-0263-0.

Bassett, R., Cai, X.-M., Chapman, L., Heaviside, C. and Thornes, J.E. (2017b) Methodology to separate urban from regional heat advection by use of the Weather Research and Forecasting mesoscale model. *Quarterly Journal of the Royal Meteorological Society*, 143, 2016–2024. https://doi.org/10.1002/qj.3062.

Birmingham City Council. (2011) 2011 census: key statistics for Birmingham and it's constituent areas. Available at: https://www.birmingham.gov.uk/downloads/file/4573/census_2011_ks101_usual_resident_populationpdf [Accessed October 6, 2017].

Bornstein, R. and Lin, Q.L. (2000) Urban heat islands and summertime convective thunderstorms in Atlanta: three case studies. *Atmospheric Environment*, 34(3), 507–516. https://doi.org/10.1016/S1352-2310(99)00374-X.

Brandsma, T. and Wolters, D. (2012) Measurement and statistical modeling of the urban heat island of the city of Utrecht (The Netherlands). *Journal of Applied Meteorology and Climatology*, 51, 1046–1060. https://doi.org/10.1175/JAMC-D-11-0206.1.

Brandsma, T., Konnen, G.P. and Wessels, H.R.A. (2003) Empirical estimation of the effect of urban heat advection on the temperature series of De Bilt (The Netherlands). *International Journal of Climatology*, 23, 829–845. https://doi.org/10.1002/joc.902.

Chapman, L., Azevedo, J.A. and Prieto-Lopez, T. (2013) Urban heat and critical infrastructure networks: a viewpoint. *Urban Climate*, 3, 7–12. https://doi.org/10.1016/j.uclim.2013.04.001.

Chapman, L., Muller, C.L., Young, D.T., Warren, E.L., Grimmond, C.S.B., Cai, X.-M. and Ferranti, J.S. (2014) The Birmingham urban climate laboratory: an open meteorological testbed and challenges of the smart city. *Bulletin of the American Meteorological Society*, 96, 1545–1560. https://doi.org/10.1175/BAMS-D-13-00193.1.

Chen, F., Kusaka, H., Bornstein, R., Ching, J., Grimmond, C.S.B., Grossman-Clarke, S., Loridan, T., Manning, K.W., Martilli, A., Miao, S., Sailor, D., Salamanca, F.P., Taha, H., Tewari, M., Wang, X., Wyszogrodzki, A.A. and Zhang, C. (2011) The integrated WRF/urban modelling system: development, evaluation, and applications to urban environmental problems. *International Journal of Climatology*, 31, 273–288. https://doi.org/10.1002/joc.2158.

Chou, M.-D. and Suarez, M.J. (1994) *An efficient thermal infrared radiation parameterization for use in general circulation models*. Greenbelt, MD: NASA Goddard Space Flight Center, NASA Technical Memorandum 104606, 85 pp.

Chow, W.T.L. and Roth, M. (2006) Temporal dynamics of the urban heat island of Singapore. *International Journal of Climatology*, 26(15), 2243–2260. https://doi.org/10.1002/joc.1364.

Dirks, R.A. (1974) Urban atmosphere: warm dry envelope over St Louis. *Journal of Geophysical Research*, 79, 2156–2202. https://doi.org/10.1029/JC079i024p03473.

Dixon, P.G. and Mote, T.L. (2003) Patterns and causes of Atlanta's urban heat Island-initiated precipitation. *Journal of Applied Meteorology*, 42(9), 1273–1284. https://doi.org/10.1175/1520-0450(2003)042<1273:PACOAU>2.0.CO;2.

Dou, J., Wang, Y., Bornstein, R. and Miao, S. (2015) Observed spatial characteristics of Beijing urban climate impacts on summer thunderstorms. *Journal of Applied Meteorology and Climatology*, 54, 94–105. https://doi.org/10.1175/JAMC-D-13-0355.1.

Ferranti, E., Chapman, L., Lowe, C., McCulloch, S., Jaroszweski, D. and Quinn, A. (2016) Heat-related failures on southeast England's railway network: insights and implications for heat risk management. *Weather, Climate and Society*, 8, 177–191. https://doi.org/10.1175/WCAS-D-15-0068.1.

Gedzelman, S.D., Austin, S., Cernak, R., Stefano, N., Partridge, S., Quesenberry, S. and Robinson, D.A. (2003) Mesoscale aspects of the urban heat island around New York City. *Theoretical and Applied Climatology*, 75, 29–42. https://doi.org/10.1007/s00704-002-0724-2.

Heaviside, C., Cai, X.-M. and Vardoulakis, S. (2015) The effects of horizontal advection on the urban heat Island in Birmingham and the West Midlands, United Kingdom during a heatwave. *Quarterly Journal of the Royal Meteorological Society*, 141, 1429–1441. https://doi.org/10.1007/s10546-012-9705-x.

Heaviside, C., Vardoulakis, S. and Cai, X.-M. (2016) Attribution of mortality to the urban heat island during heatwaves in the West Midlands, UK. *Environmental Health*, 15, 27. https://doi.org/10.1186/s12940-016-0100-9.

Jauregui, E. (1997) Heat island development in Mexico City. *Atmospheric Environment*, 31(22), 3821–3831. https://doi.org/10.1016/S1352-2310(97)00136-2.

Kalnay, E. and Cai, M. (2003) Impact of urbanization and land-use change on climate. *Nature*, 423, 528–531. https://doi.org/10.1016/j.uclim.2013.04.00.1.

Koopmans, S., Theeuwes, N.E., Steeneveld, G.J. and Holtslag, A.A.M. (2015) Modelling the influence of urbanization on the 20th century temperature record of weather station De Bilt (The Netherlands). *International Journal of Climatology*, 35, 1732–1748. https://doi.org/10.1002/joc.4087.

Loridian, T., Lindberg, F., Jorba, O., Kotthaus, S., Grossman-Clarke, S. and Grimmond, C.S.B. (2013) High resolution simulation of the variability of surface energy balance fluxes across central London with urban zones for energy partitioning. *Boundary-Layer Meteorology*, 147, 493–523. https://doi.org/10.1007/s10546-013-9797-y.

Lowry, W.P. (1977) Empirical estimation of urban effects on climate: a problem analysis. *Journal of Applied Meteorology*, 16, 129–135. https://doi.org/10.1175/1520-0450(1977)016<0129:EEOUEO>2.0.CO;2.

Martilli, A. (2002) Numerical study of urban impact on boundary layer structure: sensitivity to wind speed, urban morphology, and rural soil moisture. *Journal of Applied Meteorology*, 41(12), 1247–1266. https://doi.org/10.1175/15200450(2002)041<1247:NSOUIO>2.0.CO;2.

Mlawer, E.J., Taubman, S.J., Brown, P.D., Iacono, M.J. and Clough, S.A. (1997) Radiative transfer for inhomogeneous atmospheres: RRTM, a validated correlated-k model for the longwave. *Journal of Geophysical Research*, 102, 16663–16682. https://doi.org/10.1029/97JD00237.

Muller, C.L., Chapman, L., Grimmond, C.S.B., Young, D.T. and Cai, X.-M. (2013) Toward a standardized metadata protocol for urban meteorological networks. *Bulletin of the American Meteorological Society*, 94, 1161–1185. https://doi.org/10.1175/BAMS-D-12-00096.1.

Oke, T.R. (1973) City size and the urban heat island. *Atmospheric Environment*, 7, 769–779. https://doi.org/10.1016/0004-6981(73)90140-6.

Oke, T.R. (1982) The energetic basis of the urban heat island. *Quarterly Journal of the Royal Meteorological Society*, 108, 1–24. https://doi.org/10.1002/qj.49710845502.

Park, H.-S. (1986) Features of the heat island in Seoul and its surrounding cities. *Atmospheric Environment*, 20(10), 1859–1866. https://doi.org/10.1016/0004-6981(86)90326-4.

Parker, D. and Horton, B. (2005) Uncertainties in central England temperature 1878–2003 and some improvements to the maximum and minimum series. *International Journal of Climatology*, 25, 1173–1188. https://doi.org/10.1002/joc.1190.

Runnalls, K.E. and Oke, T.R. (2000) Dynamics and controls of the near-surface heat island of Vancouver, British Columbia. *Physical Geography*, 21(4), 283–304. https://doi.org/10.1080/02723646.2000.10642711.

Santamouris, M. (2015) Analyzing the heat island magnitude and characteristics in one hundred Asian and Australian cities and regions. *Science of the Total Environment*, 512, 582–598. https://doi.org/10.1016/j.scitotenv.2015.01.060.

Santamouris, M., Papanikolaou, N., Livada, I., Koronakis, I., Georgakis, C., Argiriou, A. and Assimakopoulos, D.N. (2001) On the impact of urban climate on the energy consumption of buildings. *Solar Energy*, 70(3), 201–216. https://doi.org/10.1016/S0038-092X(00)00095-5.

Shepard, J.M., Pierce, H. and Negri, A.J. (2002) Rainfall modification by major urban areas: observations from spaceborne rain radar on the TRMM satellite. *Journal of Applied Meteorology*, 41(7), 689–701. https://doi.org/10.1175/1520-0450(2002)041<0689:RMBMUA>2.0.CO;2.

Skamarock, W.C., Klemp, J.B., Dudhia, J., Gill, D.O., Barker, D.M., Duda, M.G., Huang, X.-Y., Wang, W. and Powers, J.G. (2008) *A description of the advanced research WRF version 3*. Boulder, CO: NCAR. NCAR technical note NCAR/TN-475+STR. https://doi.org/10.5065/D68S4MVH.

Steeneveld, G.J., Koopmans, S., Heusinkveld, B.G., van Hove, L.W.A. and Holtslag, A.A.M. (2011) Quantifying urban heat island effects and human comfort for cities of variable size and urban morphology in The Netherlands. *Journal of Geophysical Research*, 116, D20129. https://doi.org/10.1029/2011JD015988.

Stone, B., Hess, J.J. and Frumkin, H. (2010) Urban form and extreme heat events: are sprawling cities more vulnerable to climate change than compact cities? *Environmental Health Perspectives*, 118(10), 1425–1428. https://doi.org/10.1289/ehp.0901879.

Tewari, M., Chen, F., Wang, W., Dudhia, J., LeMone, M.A., Mitchell, K., Ek, M., Gayno, G., Wegiel, J. and Cuenca, R.H. (2004) Implementation and verification of the unified NOAH land surface model in the WRF model. In: 20th Conference on Weather Analysis and Forecasting/16th Conference on Numerical Weather Prediction, pp. 11–15.

Theeuwes, N.E., Solcerová, A. and Steeneveld, G.J. (2013) Modeling the influence of open water surfaces on the summertime temperature and thermal comfort in the city. *Journal of Geophysical Research: Atmospheres*, 118, 8881–8896. https://doi.org/10.1002/jgrd.50704.

Unger, J., Sumeghy, Z., Szegedi, S., Kiss, A. and Geczi, R. (2010) Comparison and generalisation of spatial patterns of the urban heat island based on normalized values. *Physics and Chemistry of the Earth*, 35, 107–114. https://doi.org/10.1016/j.pce. 2010.03.001.

Warren, E.L., Chapman, L., Young, D.T., Muller, C.L., Grimmond, C.S.B. and Cai, X.-M. (2016) The Birmingham urban climate laboratory—a high density, urban meteorological dataset, from 2012–2014. *Scientific Data*, 3, 160038. https://doi.org/10.1038/sdata.2016.38.

Wickham, C., Rohde, R., Muller, R.A., Wurtele, J., Curry, J., Groom, D., Jacobsen, R., Rosenfeld, A. and Mosher, S. (2013) Influence of urban heating on the global temperature land average using rural sites identified from MODIS classifications: an overview. *Geoinformatics and Geostatistics*, 1, 2. https://doi.org/10.4172/2327-4581.1000104.

Wong, K.K. and Dirks, R.A. (1978) Mesoscale perturbations on airflow in the urban mixing layer. *Bulletin of the American Meteorological Society*, 17, 677–688. https://doi.org/10.1175/1520-0450(1978)017<0677:MPOAIT>2.0.CO;2.

How to cite this article: Bassett R, Cai X-M, Chapman L, Heaviside C, Thornes JE. Semi-idealized urban heat advection simulations using the Weather Research and Forecasting mesoscale model. *Int J Climatol*. 2018;1–14. https://doi.org/10.1002/joc.5885